Liquid Crystals
Publication details, including instructions for authors and subscription information:
http://www.informaworld.com/smpp/title~content=t713926090

Quantitative conoscopic imaging of cholesteric thin films

K. Bjorknas[a]; M. A. Geday[b]; E. P. Raynes[a]
[a] Department of Engineering Science Oxford University Parks Road Oxford OX1 3PJ UK, [b] Oxford Cryosystems Ltd 3 Blenheim Office Park Lower Road Long Hanborough Oxford OX29 8LN UK,

Online publication date: 11 November 2010

To cite this Article Bjorknas, K. , Geday, M. A. and Raynes, E. P.(2003) 'Quantitative conoscopic imaging of cholesteric thin films', Liquid Crystals, 30: 8, 889 — 897
To link to this Article: DOI: 10.1080/0267829031000136048
URL: http://dx.doi.org/10.1080/0267829031000136048

LIQUID CRYSTALS, VOL. 30, NO. 8, AUGUST, 2003, 889–897

Taylor & Francis
Taylor & Francis Group

Quantitative conoscopic imaging of cholesteric thin films

K. BJORKNAS, M. A. GEDAY†* and E. P. RAYNES
Department of Engineering Science, Oxford University, Parks Road, Oxford OX1 3PJ, UK
†Oxford Cryosystems Ltd, 3 Blenheim Office Park, Lower Road, Long Hanborough, Oxford OX29 8LN, UK

(*Received 4 October 2002; in final form 24 March 2003; accepted 30 March 2003*)

The periodic helical structure of an aligned polymerized cholesteric liquid crystal (ChLC) film gives rise to circular Bragg reflection within a narrow wavelength range, such that circularly polarized light of the same handedness as the helix is reflected, while counter circularly polarized light is transmitted. The ChLC is also strongly optically active with opposite rotatory power at either side of the circular Bragg zone. Both the selective reflection of circularly polarized light within the Bragg zone, as well as the optical activity of the cholesteric liquid crystal, are imaged with a new conoscopic technique based on a microscope equipped with the rotating polarizer–circular analyser MetriPol imaging system. The conoscopic images reveal the off-axis Bragg zone as an annulus at wavelengths below normal selective reflection. The annulus converges into a disk before disappearing at wavelengths above the region for normal selective reflection. The technique allows clear identification of the Bragg zone and the sign of the optical activity.

1. Introduction

There are various kinds of helically ordered, unidimensionally periodic materials that give rise to circular Bragg reflection when the pitch of the helix is comparable to the wavelength of light [1–3]. One such periodic chiral structure can be found in chiral nematic (cholesteric) liquid crystals (ChLCs). For light at normal incidence, a ChLC is a 1D photonic band gap [4] material in which circularly polarized light of the same handedness as the chiral structure cannot propagate within a narrow reflection band. A cross-sectional layer of a ChLC has the orientational order of a nematic LC, but the local director, **n**, rotates around a single axis (the helix axis), making a rotation of 360° over the distance called the pitch, P. The periodic modulation of the dielectric constants gives rise to a phase grating through the thickness of the layer with a period equal to half the helical pitch length. It has previously been shown that Kossel diagrams measured in reflection make it possible to determine the pitch and the refractive indices of a chiral liquid crystal [5–7]. Here we image light transmitted through a polymerized ChLC with a conoscopic rotating polarizer technique at wavelengths spanning the visible spectrum. The uniaxially symmetric birefringence signal is separated from orientational and surface alignment effects and the derived information is directly applicable to the calculation of the pitch and the refractive indices of the cholesteric sample. Airy spirals [8] clearly present in the conoscopic images also provide an easy way of determining the handedness of the optical rotation.

2. Theoretical background

Analytic expressions describe the normal incidence optical properties of ChLCs [9], this being the only example of a simple exact solution of Maxwell's equations for periodic media [10]. Normally incident circularly polarized light with the same handedness as the helix undergoes circular Bragg reflection. The width of the reflection band is given by

$$\lambda_{\max} - \lambda_{\min} = \Delta n P \tag{1}$$

where Δn is the birefringence of the material and $\lambda_{\max} = n_{\parallel} P$ and $\lambda_{\min} = n_{\perp} P$, where $n_{\parallel}$ and $n_{\perp}$ are extraordinary and ordinary refractive indices of the LC†. At an oblique angle θ the optical properties become considerably more complicated, with the central reflection wavelength moving towards shorter wavelengths roughly as $\lambda = \lambda_0 \cos\theta$, where λ_0 is in the middle of the normal Bragg zone. Various numerical approaches for determining the propagation of light at

*Corresponding author

†We use $n_{\parallel}$, $n_{\perp}$ and Δn when discussing refractive indices due to the LC molecules and n_e and n_0 when discussing refractive indices of the assembled helical LC.

Liquid Crystals ISSN 0267-8292 print/ISSN 1366-5855 online © 2003 Taylor & Francis Ltd
http://www.tandf.co.uk/journals
DOI: 10.1080/0267829031000136048

oblique incidence have been developed by several authors [11–17]. At oblique incidence higher orders of reflection appear, at frequencies that are multiples of the Bragg frequency. Higher order reflections show separate bands reflecting specific or all polarizations. The first order reflection also develops a region of total reflection in the middle of the selective reflection band [18, 19].

In the planar aligned cholesteric structure, the difference in phase velocities of right circularly polarized (RCP) and left circularly polarized (LCP) light is very large in the selective reflection band and the optical activity arising from the helical arrangement of the molecules is much bigger than intrinsic optical activity (the chirality of the individual molecules gives non-negligible effects only when the pitch is comparable to the molecular size). The optical rotatory power ρ, is given by

$$\rho = \frac{\pi}{\lambda}(n_R - n_L) \tag{2}$$

where n_R is the refractive index for RCP light and n_L for LCP light. For wavelengths shorter than the middle of the Bragg zone, $n_R > n_L$ whereas the situation is reversed on the longer wavelength side. Use of the rotating polarizer technique, with its ability to illustrate the handedness of the optical activity [20], emphasizes this change of sign.

Reflection from a ChLC sample occurs according to two mechanisms [10], and results in reflected waves, which can interfere with each other. The first is the ordinary reflection caused by the jump in the dielectric constant at the interface between the ChLC sample and glass or air. The second is the circular Bragg reflection, due to the presence of the chiral structure in the sample. The phase of the Bragg reflected component changes by 180° across the Bragg zone implying that the interference between the Bragg and dielectrically reflected light waves varies over the Bragg zone. When linearly polarized light is incident on the ChLC sample the interference pattern not only changes within the Bragg zone but also varies strongly as a function of the orientation of the incident linearly polarized light. The angle between the director at the surface of the ChLC and the orientation of the linearly polarized light will be called α and we will use the term selective reflection variation (SRV) to describe the variation in light transmittance with respect to α.

Bragg scattering, or Kossel lines can be seen in the conoscopic image in a conventional microscope. Conoscopic images are formed using crossed polarizers and strongly convergent light through the sample, while bringing the back-focal plane of the objective to focus at the eyepiece using a Bertrand lens.

In an LC cell it is important to distinguish between the intrinsic birefringence of the bulk LC phase and the effective birefringence of the helical LC assembly. In a ChLC the molecules are aligned with their long axes perpendicular to the helical axis of the assembly. Hence the extraordinary refractive index of the helical assembly will correspond to the ordinary refractive index of the bulk phase. The ordinary refractive index of the helical assembly corresponds to an average of the two refractive indices of the bulk phase, and in summary [21]

$$n_e = n_\perp$$
$$n_o = \left[\frac{1}{2}\left(n_\perp^2 + n_\parallel^2\right)\right]^{\frac{1}{2}}. \tag{3}$$

It is clear from this approximation that we can expect to have the opposite sign of birefringence of the helical assembly relative to that of the bulk phases, as well as a reduction in the birefringence.

Inside the Bragg zone we will see no macroscopic linear birefringence, since the LC allows only one circular polarization through, and hence transmits 50% of the light intensity independently of the orientation of the polarization of the incoming light (α). Therefore the Bragg zone should appear as an area of zero birefringence ($|\sin\delta| = 0$, see later). The presence of the SRV complicates the above measurement and it becomes necessary to correct therefore, by making two measurements, one with the analyser in the light path and one without. By making this correction (as described later and in the appendix), it becomes possible to image the birefringence signal together with the optical activity alone.

The birefringence and the optical activity can be expected to show radial/tangential symmetry in the conoscopic image, depending only on the radial vector relative to the helicoidal axis. The SRV, on the other hand, depends on the angular orientation of the rubbing direction of the sample and will show no symmetric relationship to the helicoidal axis. Measurements of the combined SRV and birefringence will reflect this non-rotational symmetry, and the correction can easily be evaluated by the extent to which it eliminates this feature.

3. Experimental technique

The rotating polarizer technique (figure 1) in its commercial form (MetriPol [22]) was initially developed as a tool to image spatial variation of birefringence within a sample [20, 23]. However, as has already been illustrated in crystallographic applications, by using the technique in a conoscopic set-up, further information

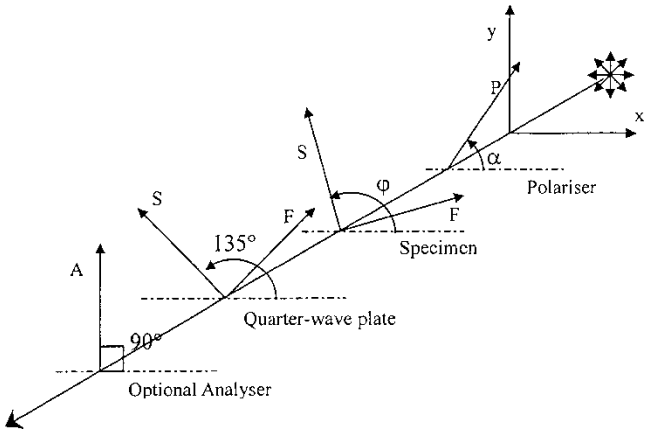

Figure 1. Light path of the rotating polarizer. The monochromatic light is modulated by the variation in the orientation of the polariser P (α); φ denotes the inclination of the slow axis in the sample. The analyser A, is oriented at 45° to the axes of the quarter-wave plate $\lambda/4$, to create a circular analyser needed for the birefringence measurements. F and S denote fast and slow axis respectively.

can be deduced regarding the optical activity and alignment of the sample [20].

The light intensity in a set-up as described in figure 1 will vary with the polariser orientation (α) as a harmonic function around an average intensity with an angular offset and an amplitude depending on the character of the sample and whether or not the analyser is inserted in the lightpath. The MetriPol software separates and images the variation in transmission intensity I, into an average intensity $I_0/2$, amplitude and an angular offset. Using the normal implementation in the study of purely birefringent samples, the intensity varies as follows [23]:

$$I = \frac{1}{2} I_0[1 + \sin 2(\alpha - \varphi) \sin \delta] \quad (4)$$

where I_0 is the total light intensity transmitted by the sample, φ is the inclination of the slow axis relative to an offset and δ is the phase difference introduced between the fast and the slow light wave within the sample for a given orientation of the incoming light,

$$\delta = \frac{2\pi}{\lambda}(n_2 - n_1) \quad (5)$$

where n_1 and n_2 are the effective refractive indices. In a uniaxial sample one of the indices, n_0 will stay constant; the other, $n_c(\theta)$, will vary with the angle between the optical axis and the incoming light vector.

If I_0 is independent of α, the technique measures the birefringence within the sample, by assigning the amplitude to $|\sin \delta|$ and the offset to orientation of the slow axis (φ). We are using the simple assumption that the ChLC assembly is optically equivalent to a two-layer structure. One layer is reflecting, and responsible for the SRV effect; the other layer is uniaxially birefringent. As discussed previously, the reflection and hence also the transmission of light will depend on α. Such transmission behaviour is characteristic for dichroic materials and the first layer will be treated as such (when looking at the transmission of light it is unnecessary to distinguish between absorption and reflection).

The SRV of a sample can be measured by measuring the intensity variation of the light transmitted by the sample as a function of α, without having an analyser in the light path. Using Jones matrices the intensity variation of the two-layer structure is easily cast as (see the appendix):

$$I_{out} = I_{in} \frac{\cosh \varepsilon}{\exp \varepsilon}[1 + \cos 2(\alpha - \varphi_{SRV}) \tanh \varepsilon] \quad (6)$$

where I_{in} is the intensity of the incoming light, and ε describes the partial reflection coefficient as a function of incoming polarization:

$$I_{min} = \exp(-\varepsilon) I_{max} \quad (7)$$

I_{max} is the intensity of the most transmitted polarization oriented at φ_{SRV} and I_{min} is the intensity of the least transmitted polarization perpendicular thereto. This variation is due partly to the selective reflection from the liquid crystal and partly to the oblique angle of incidence that causes the different polarizations to be transmitted differently by the set-up. As stated previously, ignoring the SRV effect, the intensity of the transmitted light inside the Bragg zone should not depend on α, and thus, referring to equation (4), $|\sin \delta| = 0$. Hence, by imaging the birefringence of the sample the Bragg zone can be seen in transmission as a zone of $|\sin \delta| = 0$. However, while the SRV can be measured separately, the birefringence can only be calculated by removing the SRV effect on the measurements with the analyser in the light path as described in the appendix.

The actual implementation (figure 2) of the MetriPol imaging system used here is on a JenaPol microscope (Carl Zeiss, Jena) using 10 nm interference filters and a 50x 0.95 numerical aperture (NA) objective. Large NA optics can cause distortions in the back focal plane of the objective but it has been shown using even higher aperture optics (NA up to 1.3) that although present, and increasing with angle, the distortions can be ignored [24].

4. Material and sample preparation

The material used is a chiral reactive mesogen (RM), which consists of a liquid crystalline (mesogenic) core with reactive acrylate end groups that can be polymerized

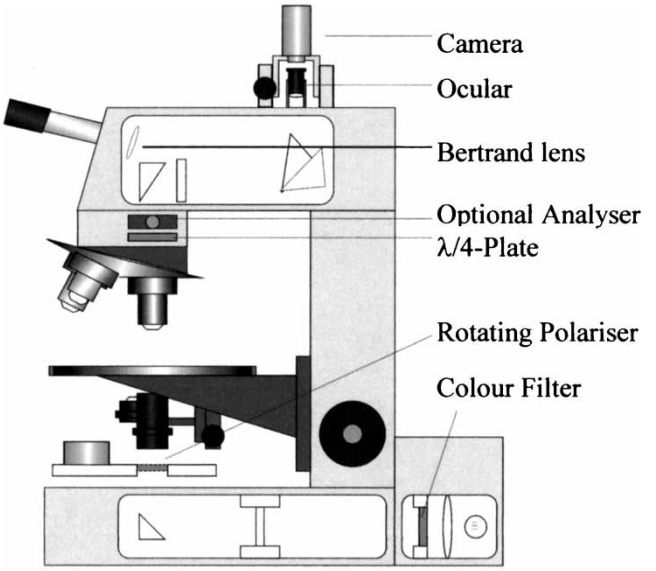

Figure 2. Conoscopic imaging is achieved with a rotating linear polarizer and a circular analyser. The conoscopic images are created by inserting a Bertrand lens in the lightpath.

to form an anisotropic solid with ordering equivalent to a ChLC. Right-handed cholesteric acrylate mixtures from Merck Specialty Chemicals Ltd were polymerized by UV radiation to produce solid films that selectively reflect a narrow band of RCP light. The RM mixtures contain a nematic host together with varying amounts of a chiral dopant to give a particular pitch. Two different RM mixtures (RMM13, and RMM11) were mixed together to give selective reflection over 525–572 nm.

Cells were fabricated using two ITO-coated glass plates. These were mechanically and chemically cleaned before coating with polyimide 2555, followed by baking in an oven and rubbing in one direction with a conventional rubbing machine. The thickness of the cell was controlled by 10 μm spacers and confirmed by measuring the interference fringes caused by the air gap. The RM host was melted and the mixture capillary filled into the cells; it was found to adopt a good planar texture provided it was heated above the clearing temperature before filling. The RM host was subsequently polymerized by exposure to a broadband UV lamp with maximum emission at 365 nm and an intensity of $0.6\,\mathrm{W\,cm^{-2}}$ for 1 min. The upper glass substrate was subsequently removed by cleaving, to enable focusing onto the back focal plane with the high NA lens.

Although the samples were well aligned they were not monodomain samples, as can be seen in the orthoscopic image in figure 3. The domains were

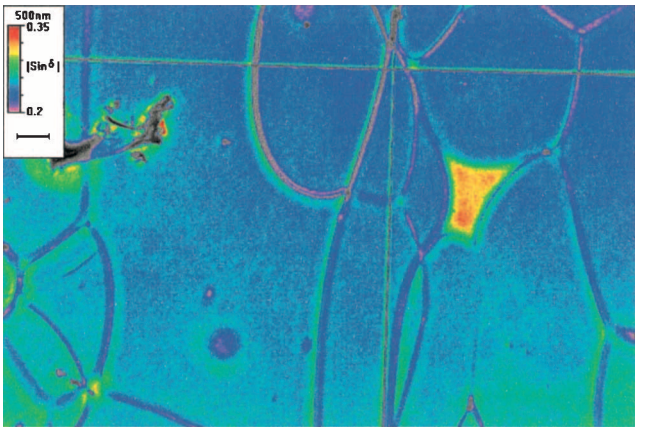

Figure 3. Orthoscopic SRV plot of the sample showing domains of approximately $1000\mu m^2$.

roughly $1000\,\mu m^2$ and the area imaged was $250 \times 175\,\mu m^2$.

5. Results: conoscopic imaging of Bragg region and demonstration of the Airy spiral

Since conoscopic images are created by interference between light rays passing obliquely through a sample it is important to consider the off-axis optics of cholesterics. Off-axis at an angle θ to normal incidence, the region for selective reflection moves to smaller wavelengths. This blue shift is demonstrated in figure 4, which shows the experimental transmission of RCP light through the right-handed sample with three different angles. Light from a xenon light-bulb was circularly polarized by a linear polarizer and a Fresnel Rhomb, and was incident onto the sample which could be rotated. The transmitted light was measured with a spectrograph coupled to a CCD. Figure 4 shows the normal ($\theta = 0°$) region for selective reflection at 525–572 nm, and the blueshift of the region for $\theta = 25°$, and

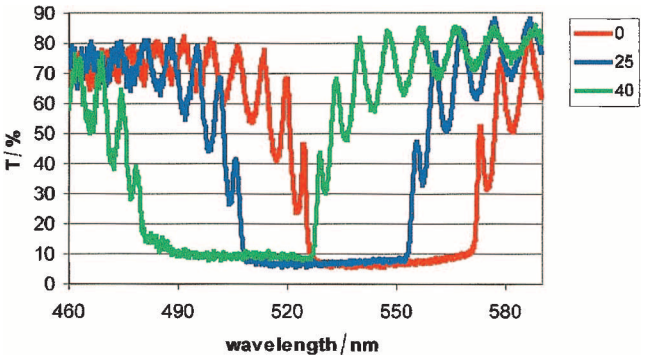

Figure 4. Off-axis transmission of RCP light at $\theta = 0°$, 25° and 40°. The selective reflection band shifts to shorter wavelengths with increasing θ (0°: 525–572nm; 25°: 504–554; 40°: 479–528nm).

$\theta = 40^\circ$. The transparency of the sample to LCP light was also confirmed although it is not shown here.

In this work a rotating linear polarizer is used for the conoscopic imaging so that the α-dependence of the transmission of linearly polarized light has to be taken into account. For unpolarized incident light, and with no analyser, the transmission spectrum of a ChLC shows the expected flat-topped selective reflection region. However, when linear polarizers or analysers are used the situation becomes much more complex, and the transmission varies strongly within the region for selective reflection. This SRV effect occurs because waves reflected from the interface due to the difference in refractive indices (between the sample and the surrounding medium) interfere with those waves experiencing circular Bragg reflection. Figure 5 shows the experimental transmission of linearly polarized light through the cholesteric sample with either the film side or the glass side facing the incident light beam. In figure 5 (*a*) the incident light faces the cholesteric film and is polarized parallel and perpendicular to the alignment direction of the surface layer, showing clear interference fringes at either side of the Bragg zone relation to the α-dependence of the phase differences between the Bragg and dielectrically reflected waves [10]. Figure 5 (*b*) compares light transmission when either the cholesteric film or the glass surface is turned towards the incident light. Since the jump in the refractive indices at the air/ChLC interface is much bigger than at the glass/ChLC interface the dielectric effect is much stronger when the cholesteric film faces the incident light. The transmission very strongly depends on the plane polarization orientation with respect to the director orientation at the surface with a variation of 40% for the air/ChLC interface and 20% for the glass/ChLC interface. Figure 5 (*b*) also reveals that there is a 65° difference in the interference pattern between either side of the sample. In the present

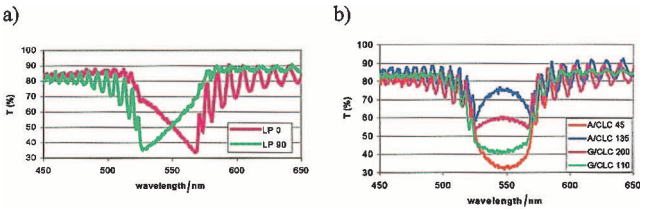

Figure 5. In the Bragg zone the transmission of linearly polarized light depends on α. (*a*) Transmission through the sample with the air/ChLC interface facing light polarized parallel ($\alpha = 0^\circ$) and perpendicular ($\alpha = 90^\circ$) to alignment direction; (*b*) comparison of air/ChLC and glass/ChLC interface transmission at ($\alpha = 45^\circ$) and ($\alpha = 135^\circ$) angles between alignment direction and polarizer.

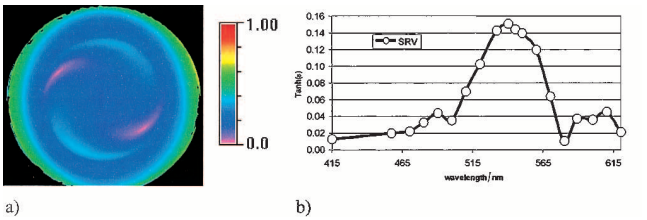

Figure 6. (*a*) Conoscopic SRV image at 530 nm; the strong signal at the periphery of the image is a consequence of variation in transmission variation of polarized light seen in high aperture objectives and the reflection of the surface of the sample. The colour key for the magnitude of the SRV effect $\tanh\varepsilon$, as in equation (6), is given on the right. (*b*) SRV magnitude measured without the circular analyser; the plotted values are taken at the centre of the conoscopic image corresponding to normal incidence.

conoscopic experiment the sample was mounted with the glass side facing the incident light.

When placing the sample in the microscope (figure 2) and removing the top analyser we image the SRV effect as a function of θ. Figure 6 (*a*) shows the variation in magnitude of the SRV effect at a wavelength just below the Bragg zone. Notice how the SRV effect adds a non-rotationally symmetric element (a spiral) to the image. The non-rotational symmetry is the result of the alignment direction of the surface layer of the sample. The spiral follows the movement when rotating the sample, showing that this is an effect due to the surface alignment direction of the sample, rather than an artifact of the technique.

Figure 6 (*b*) shows the variation of SRV with wavelength, and presents an alternative way of imaging the Bragg zone. By correcting the conoscopic images measured with the top circular analyser for the SRV effect, we remove the transmission variations due to the non-rotationally symmetric selective reflection of the linearly polarized light and any Fresnel reflection effects at the surface. The rotationally symmetric Bragg zone comes into clear view, as is shown in figure 7. The images show both the orientation as well as $\sin\delta$ at six different wavelengths, below (457, 490 and 510 nm), in (530 and 550 nm), and above (589 nm) the region for normal selective reflection. The SRV correction has eliminated the presence of the asymmetric spiral in the birefringence images, which now show the Bragg zone very clearly. Since conocopic images are created by oblique light rays, the Bragg zone can be seen at wavelengths below the region for normal selective reflection due to the off-axis blue-shift of the zone, figure 7 (*b*) 457, 490 and 510 nm. At wavelengths below normal selective reflection the Bragg zone forms an annulus with the inner edge corresponding to the

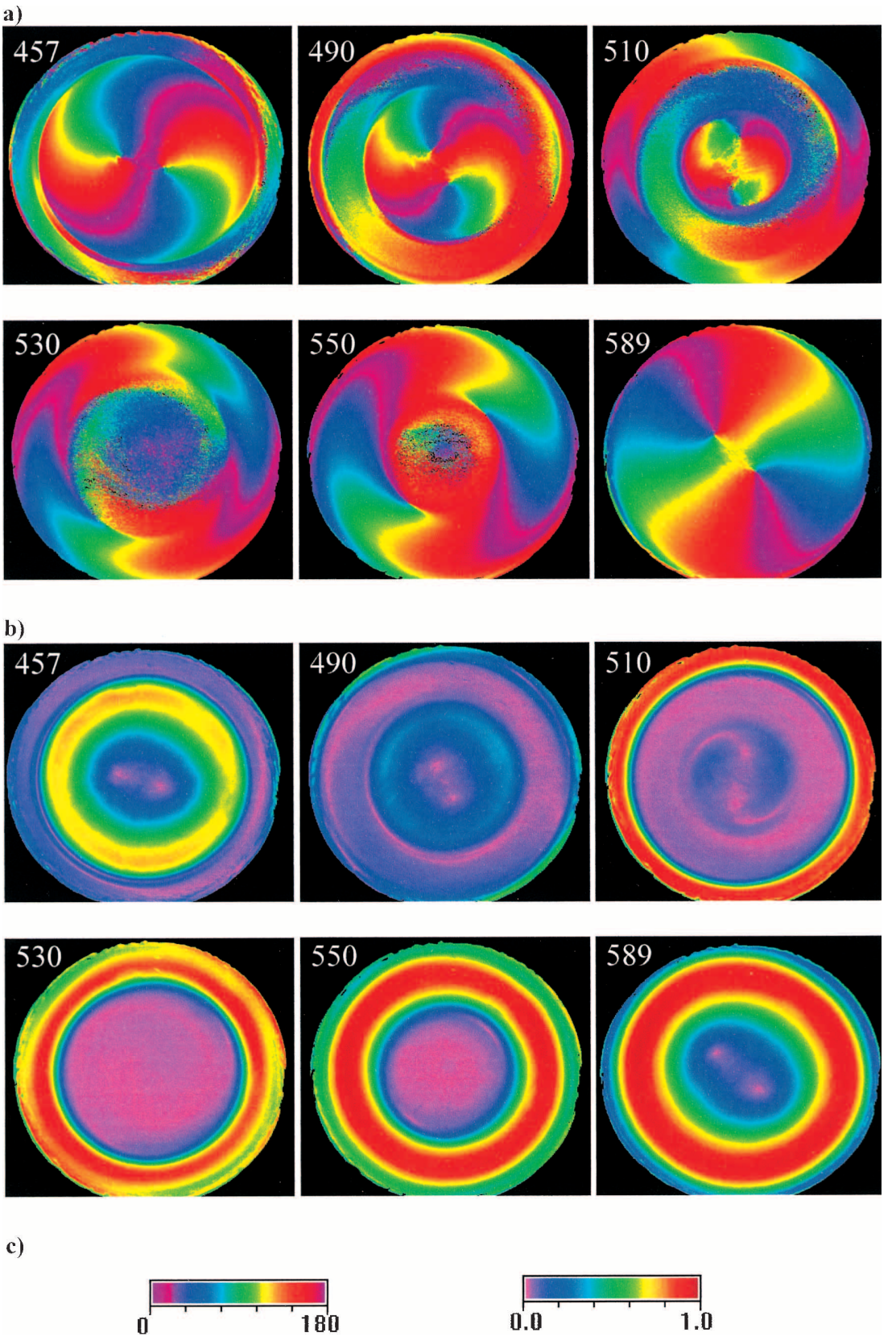

Figure 7. Conoscopic images corrected for the SRV effect at 457, 490, 510, 530, 550 and 589 nm. (*a*) Orientational images showing the optical rotation; (*b*) sin δ images giving the birefringence; (*c*) colour keys for φ and sinδ.

shorter wavelength band edge ($\lambda = n_{\perp} P \cos\theta$) whereas the outer edge corresponds to the longer wavelength band edge ($\lambda = n_{\parallel \mathrm{eff}}(\theta) P \cos\theta$, where $n_{\parallel \mathrm{eff}}$ is the effective off-axis extraordinary refractive index which varies with angle). Upon increasing the wavelength the annulus shrinks and as $\lambda_{\min}$ ($\sim$figure 7 (*b*) 530 nm) is reached the annulus collapses into a disk. At $\lambda_{\max}$ the disk disappears altogether.

Outside the Bragg zone (figure 7: 589 nm and central part of 457, 490 and 510 nm) the cell exhibits an optical character not unlike that of an ordinary solid state crystal. Looking down the helicoidal axis the birefringence is zero in the centre of the conoscopic image, where light is normal to the surface of the sample, and increases radially from the centre. The angular offset varies tangentially according to the optical activity of the cell, making Airy spirals visible [20] in the φ images, Figure 7 (*a*). The hand of each individual spiral corresponds to the hand of the optical activity of the cell. The optical rotation is of opposing directions at different sides of the Bragg zone with $\rho > 0$ for $\lambda < \lambda_0$ and $\rho < 0$ for $\lambda > \lambda_0$, in accordance with the theory for the right handed sample, equation (2). The opposite rotation direction of the Airy spiral at either side of the Bragg zone is clearly seen by comparing figure 7 (*a*) 457 nm and 589 nm.

It is possible to make simulations of the conoscopic image of the liquid crystal outside the Bragg zone using the same algorithms as used for a uniaxial crystal.

The region for total reflection, which should be visible in the middle of the Bragg zone for oblique incidence (i.e. for $\lambda < \lambda_{\min}$, 457, 490, and 510 nm in figure 7), cannot be seen because our sample is not monodomain and also because relatively broadband (10 nm) interference filters are used. The apparent biaxial split seen in some of the birefringence images in figure 7 (*b*) may be the result of accidental shearing of the sample during the removal of the upper glass cover. It may also be because of an incomplete correction for the SRV where the combination of small errors on both the SRV and the standard birefringence measurement means that these two do not exactly cancel each other out. If the sample were truly uniaxial, the birefringence in the centre would tend towards zero, thus making even the smallest error dominant.

The conoscopic images can be used to construct a stability chart as introduced by Oldano *et al.* [25], from which the pitch and refractive indices can be deduced. We introduce the parameter $m = \sin\theta$, where θ is the angle of incidence. The parameter m is measured directly from the conoscopic images as the radial distance of the Bragg edge from the centre. Plotting m^2 for the two edges of the Bragg zone as a function of λ^2 gives linear plots, as can be seen in figure 8. The

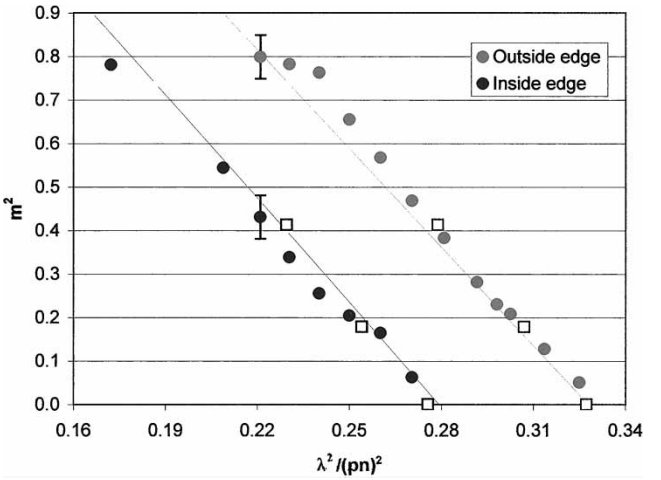

Figure 8. Location of Bragg zone measured experimentally from conoscopic images (dots). The measured values are compared with theory (solid lines) and transmission measurements (squares). The experimental error is shown for one measurement.

stability plot allows the measurement of the pitch and the refractive indices of the sample since

$$m^2 = n^2 - \frac{\lambda^2}{p^2}. \tag{8}$$

For the inner edge of the annulus this equation is exact since $n = n_{\perp}$, whereas the outer edge is more complicated because the off-axis extraordinary index varies with angle. The data obtained from the conoscopic images is plotted in a stability chart together with transmission data (from figure 4) and curves calculated from the dynamic theory by Belyakov and Dmitrienko [17] in figure 8. The theoretical curves use Merck refractive index data ($n_{\perp} = 1.5$, $n_{\parallel} = 1.64$); these indices were confirmed by fitting of our transmission data by N. Roberts [26].

The measurement of m has one major source of error, namely the manual determination of the size of the Bragg zone at any given wavelength. Repeated measurements on different data sets gave a random error of no more than ± 0.05 for the individual measurement, as is shown in figure 8. The accuracy of numerical aperture of the lens, which is used for the calculation of m, could result in a systematic error, but this has, in other studies with the same apparatus, proven to be negligible [20]. The same study illustrated the reliability of the conoscopic imaging system.

The calculated and measured Bragg zone edges agree very well. The quality of data for the inside edge is, however, poorer than the quality for the outside edge. The reason for this is clearly visible in figure 7, which shows that the inside edge is less sharp, and hence less

easy to define, than the outside edge. The very good correlation between the outside edge and theory indicates that modelling based on this information might be sufficient to determine the pitch and the refractive indices.

6. Conclusions

The birefringence and optical activity of an aligned cholesteric sample have been imaged separately at wavelengths spanning and overlapping the region for normal selective reflection. The imaging technique uses a rotating polarizer, and is a quantitative method enabling the elimination of the dark cross normally present in conoscopic images. A technique for correcting for the (linear) polarization sensitivity is introduced and the corrected conoscopic image facilitates the assessment of the Bragg zone. The first order Bragg reflection appears as a single annular ring for wavelengths below—, as a disk for wavelengths within—, and disappears for wavelengths above—the region for normal selective reflection. The handedness of the Airy spiral at either side of the Bragg zone offers a direct way of determining the handedness of the ChLC. The Airy spiral shows that the optical activity is clockwise (i.e. positive and right-handed) for wavelengths shorter than the Bragg zone and negative for longer wavelengths. The pitch and refractive indices can be deduced from the edges of the Bragg annulus whereas the sign of the optical activity is determined from the handedness of the Airy spiral.

Experiments are planned to investigate higher order Bragg reflections, the regions for total reflection, and the apparent biaxial split using the MetriPol technique.

Appendix

The MetriPol data collection

We consider the liquid crystal cell to be composed of a reflective layer and a birefringent layer in series, with no symmetry restraint between the two. The light path for the SRV measurements may then be cast in terms of Jones' matrices as:

$$\boldsymbol{J}_{\text{outSRV}} = \boldsymbol{R}_{-\varphi}\boldsymbol{M}_{\delta}\boldsymbol{R}_{\varphi}\boldsymbol{R}_{-\varphi_{\text{SRV}}}\boldsymbol{M}_{\varepsilon}\boldsymbol{R}_{\varphi_{\text{SRV}}}\boldsymbol{R}_{\alpha}\boldsymbol{J}_{\text{in}} \quad \text{(A1)}$$

and for the entire light path

$$\boldsymbol{J}_{\text{out}} = \boldsymbol{M}_{\text{circ}}\boldsymbol{J}_{\text{outSRV}} \quad \text{(A2)}$$

where $\boldsymbol{J}_{\text{in}}$ represents the incident polarization, $\boldsymbol{R}_{\alpha}$ is the orientation matrix for the polarizer at an angle α, $\boldsymbol{R}_{\varphi}$ and $R_{\varphi\text{SRV}}$ are the orientation matrices for the birefringent part ($\boldsymbol{M}_{\delta}$) and the SRV part ($\boldsymbol{M}_{\varepsilon}$) of the crystal respectively, and $\boldsymbol{M}_{\text{circ}}$ the circular analyser. The resulting intensity is then found by taking the square of the length of $\boldsymbol{J}_{\text{out}}$.

We write out the matrices for the entire light path (A2):

$$\begin{aligned} J_{\text{out}} = \frac{1}{2}&\begin{bmatrix}1 & 1\\ 1 & 1\end{bmatrix}\begin{bmatrix}1 & 0\\ 0 & \text{i}\end{bmatrix}\\ &\begin{bmatrix}\cos\varphi & +\sin\varphi\\ -\sin\varphi & \cos\varphi\end{bmatrix}\begin{bmatrix}\exp(\text{i}\delta/2) & 0\\ 0 & \exp(-\text{i}\delta/2)\end{bmatrix}\\ &\begin{bmatrix}\cos\varphi & -\sin\varphi\\ +\sin\varphi & \cos\varphi\end{bmatrix}\begin{bmatrix}\cos\varphi_{\text{SRV}} & +\sin\varphi_{\text{SRV}}\\ -\sin\varphi_{\text{SRV}} & \cos\varphi_{\text{SRV}}\end{bmatrix}\\ &\begin{bmatrix}1 & 0\\ 0 & \exp(-\varepsilon)\end{bmatrix}\begin{bmatrix}\cos\varphi_{\text{SRV}} & -\sin\varphi_{\text{SRV}}\\ +\sin\varphi_{\text{SRV}} & \cos\varphi_{\text{SRV}}\end{bmatrix}\\ &\begin{bmatrix}\cos\alpha & +\sin\alpha\\ -\sin\alpha & \cos\alpha\end{bmatrix}\begin{pmatrix}E_0\\ 0\end{pmatrix}. \end{aligned} \quad \text{(A3)}$$

Inserting $\varepsilon = 0$, in equation (A3) gives us equation (4) directly; equation (6) can similarly easily be deduced using the same matrices (with $\varepsilon \neq 0$), but without the analyser.

Both equations (4) and (6) can be cast in the form of using the trigonometric addition formulae:

$$I = I_0(a_0 + a_1\sin 2\alpha + a_2\cos 2\alpha) \quad \text{(A4)}$$

where a_0, a_1 and a_2 can be deduced during data collection using a Fourier analysis [23].

The recast of equation (4) (a purely birefringent sample) becomes:

$$\begin{aligned} I = &\frac{I_0}{2}\\ &+\frac{I_0}{2}\sin\delta\cos 2\varphi\sin 2\alpha\\ &-\frac{I_0}{2}\sin\delta\sin 2\varphi\cos 2\alpha \end{aligned} \quad \text{(A5)}$$

and the values for the birefringence are easily deduced: $\sin^2\delta = (a_1^2 + a_2^2)/a_0^2$, and $\tan 2\varphi = -a_2/a_1$.

The recast of equation (6) becomes:

$$\begin{aligned} I_{\text{out}} = &\frac{I_{\text{in}}\cosh\varepsilon}{\exp\varepsilon}\\ &+\frac{I_{\text{in}}\cosh\varepsilon}{\exp\varepsilon}\tanh\varepsilon\sin 2\varphi_{\text{SRV}}\sin 2\alpha\\ &+\frac{I_{\text{in}}\cosh\varepsilon}{\exp\varepsilon}\tanh\varepsilon\cos 2\varphi_{\text{SRV}}\cos 2\alpha \end{aligned} \quad \text{(A6)}$$

and the SRV can easily be derived from the measured values of a_0, a_1 and a_2 in a similar way. Notice that the a_0 term is necessary for the normalization of a_1 and a_2.

The SRV correction.

In the following the optical activity has been ignored, since its effect appears not to have any influence on the

SRV correction. We can cast the light variation for entire light path, equation (A3), in a form similar to (A4), and get for the terms a_0, a_1 and a_2:

$$a_0 = \frac{1}{2} I_{\text{in}} \cosh\varepsilon [1 + (\sin\delta \sin 2\varphi \cos 2\varphi_{\text{SRV}} - \sin\delta \cos 2\varphi \sin 2\varphi_{\text{SRV}}) \tanh\varepsilon] \quad \text{(A7)}$$

$$a_1/I_{\text{in}} = \left(K \cos 2\varphi_{\text{SRV}} + \frac{1}{2}\right) \sin\delta \sin 2\varphi - K \sin 2\varphi_{\text{SRV}} \sin\delta \cos 2\varphi + \frac{1}{2} \sinh\varepsilon \cos 2\varphi_{\text{SRV}} \quad \text{(A8)}$$

$$a_2/I_{\text{in}} = \left(K \cos 2\varphi_{\text{SRV}} - \frac{1}{2}\cosh\varepsilon\right) \sin\delta \cos 2\varphi + K \sin 2\varphi_{\text{SRV}} \sin\delta \sin 2\varphi + \frac{1}{2} \sinh\varepsilon \sin 2\varphi_{\text{SRV}} \quad \text{(A9)}$$

where $K = \frac{1}{2}(\cosh\varepsilon - 1)\cos 2\varphi_{\text{SRV}}$.

The equations (A8) and (A9) provide two equations with two unknowns, $\sin\delta\cos(2\varphi)$ and $\sin\delta\sin(2\varphi)$, since we can measure ε and φ_{SRV} separately. However, since the measured value for a_0 has been used for the normalization of a_1 and a_2 to remove I_{in} (the light intensity I_{in} was not kept constant between the different measurements) while being dependent on the above unknown quantities, a convergent iterative process is necessary.

We thank Dr Simon Greenfield of Merck Specialty Chemicals Ltd. for providing the chiral RM mixtures. Special thanks are also due to Prof. Mike Glazer of the Clarendon Laboratory, Oxford University, for use of the microscope and constructive input. Dr Helen Gleeson of Manchester University and Dr John Lydon of Leeds University are thanked for useful discussions. K.B. gratefully acknowledges Sharp Laboratories of Europe for funding and Dr Sandra Gilmour for much support and many helpful discussions.

References

[1] Srinivasarao, M., 1999, *Chem. Rev.*, **99,** 1954.
[2] Hodgkinson, I., and Wu, O., 2001, *Adv. Mat.*, **13,** 889.
[3] Tamaoki, N., 2001, *Adv. Mat.*, **13,** 1135.
[4] For a good review on PBGs see Joannopoulos, J. D., and Meade, R. D., 1995, *Photonic Crystals Molding the Flow of Light* (Princeton University Press).
[5] Miller, R. J., Gleeson, H. F., and Lydon, J. E., 1999, *Phys. Rev. E*, **59,** 1821.
[6] Miller, R. J., Gleeson, H. F., and Lydon, J. E., 1999, *Phys. Rev. E*, **59,** 1828.
[7] Miller, R. J., Gleeson, H. F., and Lydon, J. E., 1999, *J. Phys.: Condens. Matter*, **11,** 1423.
[8] Ramachandran, G. N., and Ramaseshan, S., 1961, *Handbuch der Physik*, Vol XXV/1, pp. 1–217 (Springer Verlag).
[9] De Vries, H. L., 1951, *Acta Crystallgr.*, **4,** 219.
[10] Belyakov, V. A., 1992, *Diffraction Optics of Complex-Structured Periodic Media* (Springer Verlag).
[11] Berreman, D. W., 1972, *J. Opt. Soc. Am.*, **62,** 502.
[12] Berreman, D. W., and Scheffer, T. J., 1970, *Phys. Rev. Lett.*, **25,** 577.
[13] Dreher, R., and Meier, G., 1973, *Phys. Rev. A.*, **8,** 1616.
[14] Abdulhalim, I., Benguigui, L., and Weil, R., 1985, *J. Physique*, **46,** 815.
[15] Oldano, C., 1985, *Phys. Rev. A*, **31,** 1014.
[16] Venugopal, V. C., and Lakhtakia, A., 2000, *Proc. R. Soc. London*, **A456,** 125.
[17] Belyakov, V. A., and Dmitrienko, V. D., 1974, *Sov. Phys. – Solid State*, **15,** 1811.
[18] Takezoe, H., Ouchi, Y., Sugita, A., Hara, M., Fukuda, A., and Kuze, E., 1982, *Jpn. J. Appl. Phys.*, **21,** L390.
[19] Takezoe, H., Hashimoto, K., Ouchi, Y., Sugita, A., Hara, M., Fukuda, A., and Kuze, E., 1983, *Mol. Cryst. liq. Cryst.*, **101,** 329.
[20] Geday, M. A., and Glazer, A. M., 2002, *J. Appl. Cryst.*, **35,** 185.
[21] Muller, W., and Stegemeyer, H., 1973, *Ber. Buns.*, **77,** 20.
[22] MetriPol webpage: www.metripol.com
[23] Glazer, A. M., Lewis, J. G., and Kaminsky, W., 1996, *Proc. R. Soc. London*, **A452,** 2751.
[24] Miller, R. J., and Gleeson, H. F., 1996, *J. Phys. II Fr.*, **6,** 909.
[25] Oldano, C., Miraldi, E., and Taverna Valabrega, P., 1983, *Phys. Rev. A*, **27,** 3291.
[26] Roberts, N., Univ. of Manchester 2002, private communication.